A UV Resonance Line Echo from a Circumstellar Shell Around a Hydrogen-Poor Superluminous Supernova

R. Lunnan,[1,2*] C. Fransson,[1] P. M. Vreeswijk,[3] S. E. Woosley,[4] G. Leloudas,[5]
D. A. Perley,[6] R. M. Quimby,[7,8] Lin Yan,[9] N. Blagorodnova,[2] B. D. Bue,[10]
S. B. Cenko,[11,12] A. De Cia,[13] D. O. Cook,[2] C. Fremling,[2] P. Gatkine,[11]
A. Gal-Yam,[3] M. M. Kasliwal,[2] S. R. Kulkarni,[2] F. J. Masci,[14] P. E. Nugent,[15,16]
A. Nyholm,[1] A. Rubin,[3] N. Suzuki,[17] and P. Wozniak[18]

[1]Oskar Klein Centre, Astronomy Department, Stockholm University, SE-106 91 Stockholm, Sweden
[2]Department of Astronomy, California Institute of Technology,
1200 East California Boulevard, Pasadena, CA 91125, USA
[3]Benoziyo Center for Astrophysics and the Helen Kimmel Center for Planetary Science,
Weizmann Institute of Science, 76100 Rehovot, Israel
[4]Department of Astronomy and Astrophysics, University of California, Santa Cruz, CA 95064, USA
[5]Dark Cosmology Centre, Niels Bohr Institute,
University of Copenhagen, Juliane Maries Vej 30, DK-2100 Copenhagen, Denmark
[6]Astrophysics Research Institute, Liverpool John Moores University,
IC2, Liverpool Science Park, 146 Browlow Hill, Liverpool L3 5RF, UK
[7] Department of Astronomy, San Diego State University, San Diego, CA 92182, USA
[8] Kavli IPMU (WPI), UTIAS, The University of Tokyo, Kashiwa, Chiba 277-8583, Japan
[9]Caltech Optical Observatories & Infrared Processing and Analysis Center,
California Institute of Technology, Pasadena, CA 91125, USA
[10]Jet Propulsion Laboratory, California Institute of Technology, Pasadena, CA 91109, USA
[11]Astrophysics Science Division, NASA Goddard Space Flight Center,
Mail Code 661, Greenbelt, MD 20771, USA
[12]Joint Space-Science Institute, University of Maryland, College Park, MD 20742, USA
[13]European Southern Observatory,Karl-Schwarzschild Str. 2, 85748 Garching bei Munchen, Germany
[14]Infrared Processing and Analysis Center, California Institute of Technology, Pasadena, CA 91125, USA
[15]Lawrence Berkeley National Laboratory, 1 Cyclotron Road, MS 50B-4206, Berkeley, CA 94720, USA
[16]Department of Astronomy, University of California, Berkeley, CA 94720-3411
[17] Kavli Institute for the Physics and Mathematics of the Universe (Kavli IPMU, WPI),
University of Tokyo, 5-1-5 Kashiwanoha, Kashiwa, Chiba, 277-8583, Japan
[18] Los Alamos National Laboratory, MS-D466, Los Alamos, NM 87545, USA
* E-mail: ragnhild.lunnan@astro.su.se.

Superluminous supernovae are rare and energetic explosions, whose underlying energy source and progenitor stars are not well understood. Observing the structure of the circumstellar medium offers a powerful test of possible scenarios. A series of spectroscopic observations of the superluminous supernova iPTF16eh reveal both absorption and time-variable emission in the Mg II$\lambda\lambda$2796,2803 resonance doublet, which are naturally explained by a light echo from a circumstellar shell. Modeling the evolution of the emission, we find a shell radius of 0.1 pc and velocity of 3300 km s^{-1}, implying the shell was ejected four decades prior to the supernova explosion. These properties match theoretical predictions of pulsational pair-instability shell ejections, and imply the progenitor had a He core mass of $\sim 52\ M_{\odot}$, corresponding to an initial mass of $\sim 115\ M_{\odot}$.

”Superluminous” supernovae (SLSNe) have garnered significant attention in the past decade, as their large peak luminosities ($\sim 10^{44}$ erg s^{-1}), radiated energies ($\gtrsim 10^{51}$ erg) and long times scales cannot be easily explained by the same mechanisms that power common core-collapse and Type Ia SNe (*1, 2*). One class of models, where the spin-down of a newborn magnetar energizes the ejecta from within (e.g., (*3, 4*)), requires rapid rotation but not particularly massive progenitors compared to other stripped-envelope supernovae. Other models require the progenitor to be significantly more massive, either as pair-instability explosions of stars with initial masses $> 140\ M_{\odot}$ (*5, 6*), or through conversion of kinetic energy to radiation via interaction between the supernova ejecta and dense circumstellar material (CSM) ejected by the star in the years to decades preceding the explosion (e.g., (*7–9*)). CSM interaction is at least relevant for a subclass of SLSNe that show narrow hydrogen lines (SLSN-II); whether SLSNe without signs of hydrogen in their spectra (SLSN-I) can similarly be powered by interaction with hydrogen-free material is debated (*8, 10*). However, several processes in massive stars predict the presence of dense CSM from episodic mass loss, either from LBV-like eruptions (*?, 11*) or from shell ejections via the pulsational pair-instability (PPI) mechanism which operates in stars with helium cores in the mass range $30 - 64\ M_{\odot}$ (*7, 12*). Direct observations of CSM around SLSN-I are scarce, with the main exceptions being the late appearance of Hα emitting material detected in three SLSNe by (*13, 14*), which was interpreted as collision with a circumstellar shell. Here, we present iPTF16eh, a SLSN-I where a CSM shell is inferred through the unique observation of a resonance line light echo.

iPTF16eh was first detected by the intermediate Palomar Transient Factory (*15*) on 2015 December 17.5 (UT). An initial spectrum, taken on 2016 February 18 showed a blue continuum with shallow O II absorptions characteristic of SLSN-I (Figure 1); subsequent spectra with bluer wavelength coverage revealed two sets of narrow Mg II absorption lines. Assuming the higher-redshift absorption lines originate in the interstellar medium of the host galaxy, the redshift of iPTF16eh is $z = 0.427$. We continued to follow the evolution of iPTF16eh photometrically and spectroscopically, and find that it is among the most luminous SLSNe discovered to date with a peak absolute magnitude of $M_u = -22.55$ mag (AB) (*16, 17*), but otherwise evolves similarly to other SLSN-I with slow timescales. However, it displays one unusual feature never seen before in SLSN spectra: an intermediate-width emission feature around 2800 Å in the rest frame, also likely associated with Mg II, emerging around 100 days after explosion (taking the explosion date to be 2015 December 14.5; see SM).

The right panel of Figure 1 shows the development of the Mg II emission line in relation to the two Mg II absorption systems. The line is first clearly visible in the spectrum taken 100 days past explosion, and persists for more than 200 days, having finally faded below detectability 350 days after explosion. To quantify the properties of the line, we fit a Gaussian profile, and measure the line centroid, flux, and full-width half maximum (FWHM) as a function of time (Figure 2). The centroid of the line clearly shifts redwards with time; initially the emission line is blueshifted with respect to the supernova redshift by $\sim 1600\ \mathrm{km\,s^{-1}}$, but reaches a redshift of $\sim 2900\ \mathrm{km\,s^{-1}}$ before fading away. The line flux varies at most by a factor of two until the line starts fading, and the FWHM of the line similarly remains approximately constant around $\sim 1500\ \mathrm{km\,s^{-1}}$.

Both the blueshifted absorption system and the existence and properties of the emission line can be naturally explained by resonance line scattering of the SLSN continuum by a rapidly expanding, roughly spherical CSM shell. Mg II ions in the shell absorb continuum photons around 2800 Å from the SLSN, which we see along our line of sight as a blueshifted absorption feature in the SLSN spectrum. These excited Mg II ions then almost instantaneously (within 10^{-8} s) decay back down to the ground level, and emit a line emission photon in a random direction, which we observe as an emission line. Because the light travel time across the shell (R_{out}/c) is longer than the duration of the SLSN light causing the excitation, we see different parts of the shell light up at different times (SM Fig. 7), explaining the drift of the emission line from blueshifted to redshifted as we go from seeing the front to the back of the shell.

To quantify the shell properties, we have done Monte-Carlo calculations of the scattering process (SM), assuming a spherical shell with inner radius R_{in} and outer radius R_{out}. The size of the shell is constrained by the duration of the emission, while the thickness is determined by the relative intensity of the emission lines and the scattering continuum, $F_\nu^{\mathrm{line}}/F_\nu^{\mathrm{cont}}(t_{\mathrm{peak}}) \approx \Delta R/R$. We assume homologous expansion with $V = V_{\mathrm{max}}(r/R_{\mathrm{out}})\ \mathrm{km\,s^{-1}}$ for the shell, which is likely for a time-limited eruption, like that resulting from the 1843 eruption in Eta Carinae (*18*), or for a pulsational pair-instability ejection (*7*); however, the results are not sensitive to this assumption. In addition to the parameters describing the shell, the resulting emission depends on the light curve of the scattered radiation, i.e. the supernova continuum around 2800 Å. As our observed photometry does not extend sufficiently blue, we measure the continuum in this wavelength region from the observed spectra (Figure 4 in SM). Unfortunately, our earliest

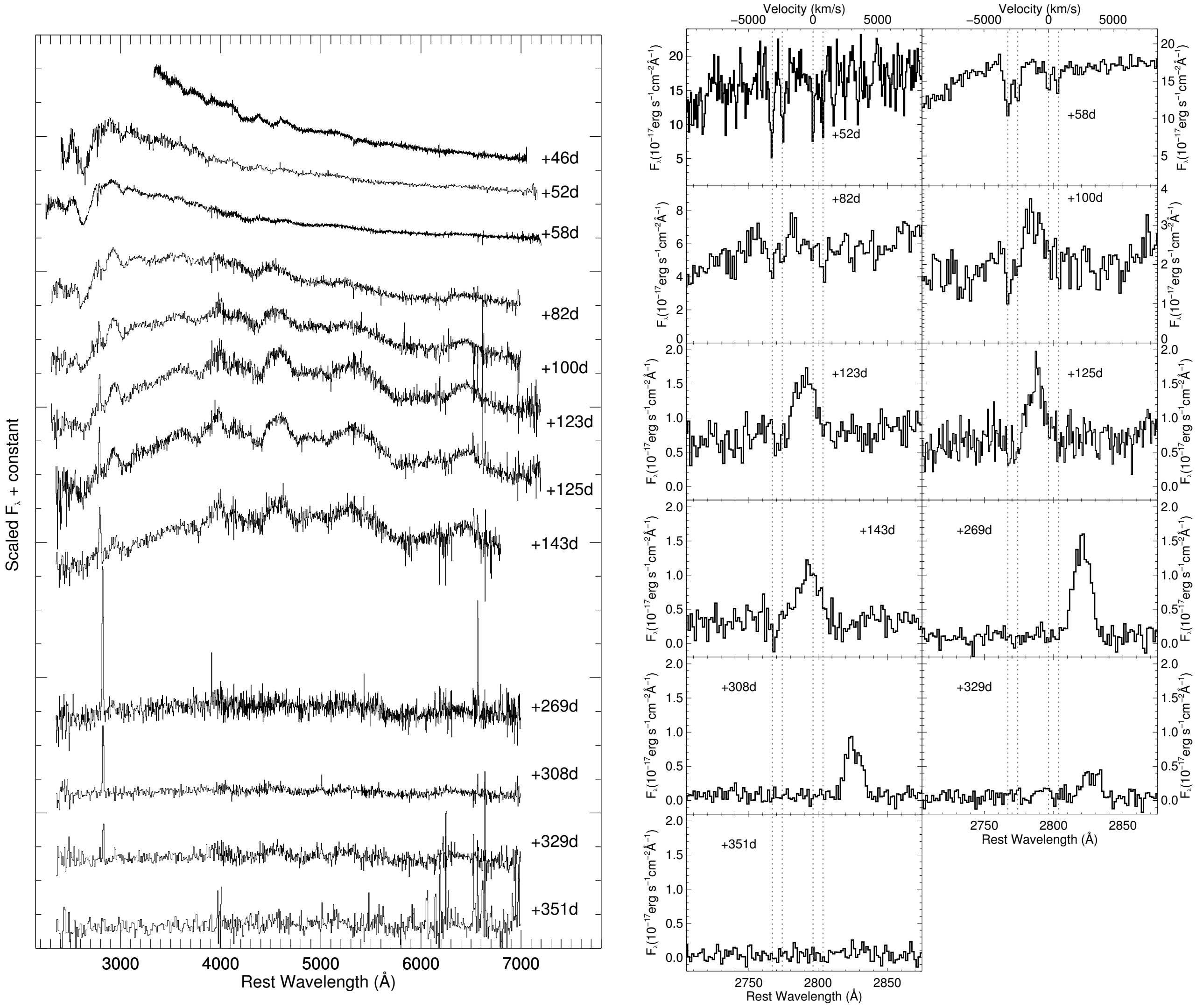

Figure 1 Spectroscopic evolution of iPTF16eh. *Left:* Observed spectroscopic sequence of iPTF16eh, with the phase of each spectrum in rest-frame days relative to the best-fit explosion date indicated. The spectroscopic evolution of iPTF16eh is similar to a typical SLSN, with the exception of a strong emission line developing around 2800 Å. Spectra have been arbitrarily scaled and binned for display purposes. *Right:* Zoom-in on the region around Mg II, shown on an absolute flux scale and without binning. The two earliest spectra clearly show the presence of two Mg II absorption systems; the highest-redshift one is one is interpreted as due to absorption in the host galaxy ISM, while the lower-redshift one is blueshifted by about 3200 $\mathrm{km\ s^{-1}}$. Note the development of an emission line around 100 days past explosion, the redward shift of the emission line with time, and its fading away at 330-350 days after explosion.

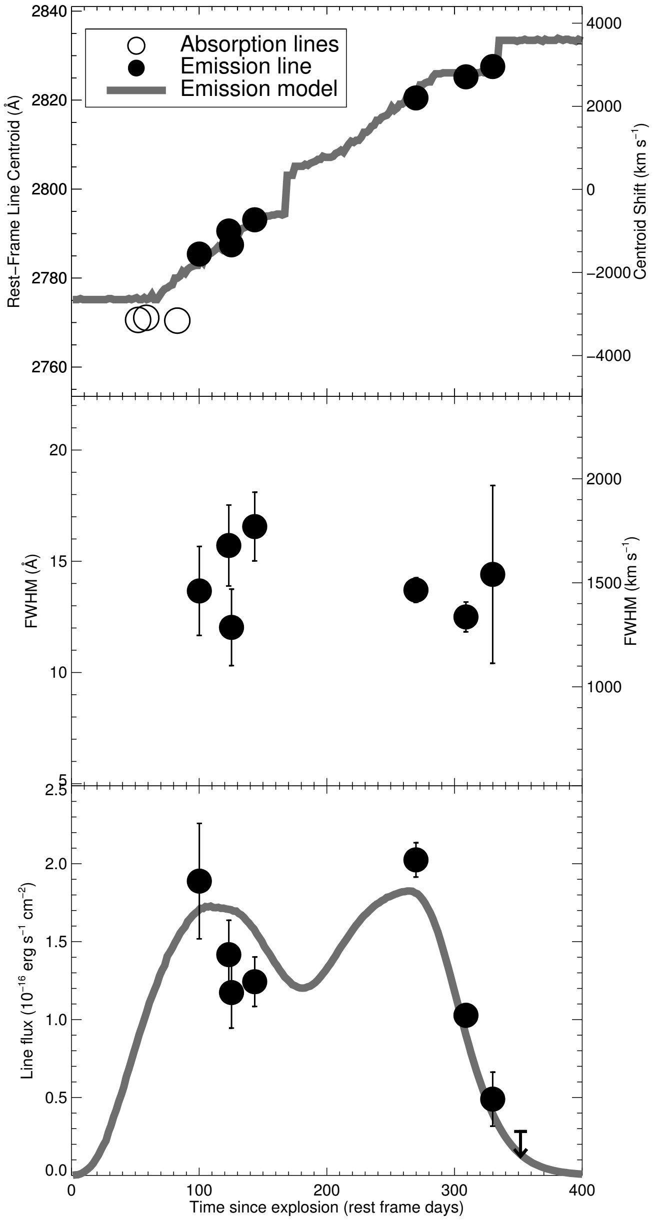

Figure 2 Observed and modeled evolution of the Mg II emission line. The black filled circles show measured line properties as measured by fitting a Gaussian profile, while the gray line shows the line evolution in the resonance scattering model. *Top:* Line centroid versus time. In addition to the filled circles showing the evolution of the emission line, the open circles show the average of the absorption line doublet, where measurable. *Center:* Line FWHM versus time. *Bottom:* Line flux versus time.

spectrum covering this wavelength region is 87 days after explosion; prior to the first spectrum, we therefore use a stretched form of the modelled UV light curve of PTF12dam (*19*), which fits the observed 2800 Å light curve after the peak (SM).

Fig. 3 shows the line profiles at the observed epochs for $R_{\rm in} = 130$ light days and $R_{\rm out} = 137$ light days and $V_{\rm max} = 3300 \ {\rm km \ s^{-1}}$, and in Fig. 2 the centroid and flux from the model. As is seen, there is a good qualitative agreement with the observed evolution in Figs. 1 and 2. In the first two epochs, the SN continuum dominates the light output, and we see strong absorption together with a weak, but growing, emission component on top of the SN spectrum. The spectrum at 143 days marks the transition from an absorption dominated to a pure emission spectrum, as the direct continuum from the SN becomes too faint to show any absorption component. The flux of the emission lines is nearly constant up to ~ 270 days, when it drops sharply, in good agreement with the observations, as the constant time parabola of the echo exits from the outer radius at the far side of the shell (Fig. 2). At 374 days only a weak emission from the scattered tail of the SN light curve remains.

The line shapes are sensitive to the input light curve, and can therefore serve as a probe of the (unobserved) early supernova light curve around 2800 Å. To explore this, we also run a model including a luminous shock breakout, parametrized as a burst of radiation at 1 day and a Gaussian shape with $\sigma = 1$ day and a peak luminosity a factor of 5 brighter than that of the main peak at the relevant wavelengths around 2800 Å. While we do not explicitly assume a temperature for this shock breakout contribution, it is implied in the model that a sufficiently small amount of the Mg II is ionized to leave the line optically thick. The bottom panel in Fig. 3 shows the result of this calculation, which leads to two distinct peaks at the long wavelength edge of the line. The width of the line peaks are mainly determined by the width of the shell, as long as the burst is short compared to the width of the shell. These examples show that the late line shape serves as a powerful diagnostic of the early light curve, and in particular that in the case of iPTF16eh the echo is consistent with being dominated by the main SN light curve.

We can also place constraints on the geometry of the shell. The smooth velocity evolution, as well as the very similar velocity of absorption ($-3,200\ \mathrm{km\ s^{-1}}$) and maximum emission ($\sim 3,400\ \mathrm{km\ s^{-1}}$) argue for a symmetric eruption. The fact that both absorption and emission lines are seen also argues against a thin ring (similar to what was seen in SN 1987A), since this would require the plane of the ring to be very close to the line of sight. Moreover, we find that the total scattered flux in the absorption components is consistent within the errors of the flux in the integrated emission (SM), suggesting that the covering factor of the shell is close to 4π steradians; the geometry is therefore consistent with a spherical shell.

As Mg II is the only line we detect from the shell, we can only place weak constraints on the composition, and therefore the total mass of the shell. The nondetection of other lines does not imply an unusual composition, as Mg II is the strongest resonance line of abundant elements in the observed part of the spectrum, and other possible species like Na I, K I and Ca II are likely ionized by the hot supernova continuum (see SM). The Mg II doublet is at least partially saturated, so the equivalent width of the Mg II$\lambda 2803$ line only allows us to set a lower limit on the column density of $N_{\mathrm{Mg\ II}} \gtrsim 10^{14}$ atoms cm^{-2}. Similarly, the lack of detected Hα emission from the shell does not necessarily imply that the shell is H-poor, but places an upper limit on the H mass of $M \lesssim 27f\ M_{\odot}$, where $f < 1$ is the filling factor of the shell (SM).

Given the derived size of $\sim 3.5 \times 10^{17}$ cm and observed velocity of $\sim 3300\ \ \mathrm{km\ s^{-1}}$, the shell was ejected ~ 32 years prior to the supernova explosion, assuming a constant velocity. We consider several different mechanisms for the origin of the shell. In the SM we rule out the wind of a Wolf-Rayet progenitor, as well as the direct collision with a CS shell.A more likely possibility is that the shell could be the result of a previous LBV ejection, similar to that seen in Eta Carinae. In particular, the eruption in ~ 1840 resulted in high velocity material moving up to $\sim 6000\ \mathrm{km\ s^{-1}}$ (*20*). In addition, the 2012A outburst of SN 2009ip shows that ejections with

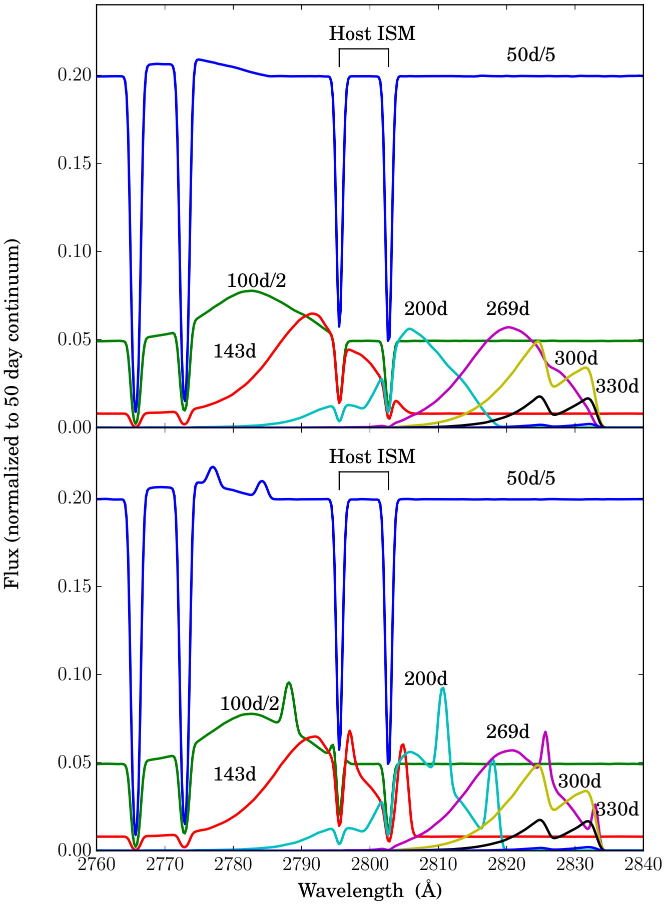

Figure 3 Time sequence of simulated spectra in the Mg II wavelength region for a shell with inner radius 130 light days and outer radius 137 light days for two different light curves for the 2800 Å flux. *Upper panel:* Our standard model, scaled to the continuum flux at 50 days. *Bottom panel:* Same as the upper panel, but with a luminous burst added at 1 day. We have added absorption lines from the host galaxy and convolved the spectrum with the instrumental resolution of the Keck/LRIS spectrograph with the grating used (FWHM ≈ 6.5 Å).

velocities of $\gtrsim 6000~\mathrm{km~s^{-1}}$ can occur without disrupting the star (*21, 22*). A problem for this scenario is that the structure of the CSM may be highly anisotropic with material moving at a range of velocities, as is seen for Eta Car (*20*), unlike the detached shell we see in iPTF16eh.

Our preferred alternative is that the shell is the result of a PPI ejection, which has been discussed in connection to both H-rich and H-poor SLSNe (*1, 7, 10, 12–14, 19*). The time scale between the first major ejection and the final collapse is a strong function of the He core mass; 32 years would correspond to a He core mass of $\sim 51 - 53~M_{\odot}$ according to (*12*). Depending on the amount of rotation this implies a zero-age main sequence mass of $\sim 90 - 120~M_{\odot}$. Ejection of $\lesssim 10~M_{\odot}$ of material in the initial pulse results in velocities $\sim 2700 - 2900~\mathrm{km~s^{-1}}$ (*12*), close to our observed velocities, and thus shows that one can get a consistent picture in this scenario. Subsequent pulses happen closer to the final collapse for cores in this mass range, and would contribute mainly to the supernova light curve as the ejecta collides with them.

Although our observations are consistent with a shell resulting from a PPI ejection, this does not imply that the supernova light curve is also explained by interaction between later shell ejections. In particular, the total energy and luminosity expected from such shell ejections are lower than what is observed for iPTF16eh (*12*). Possibilies, discussed in the SM, include magnetars in both lower mass stars and high mass stars, ending their lives as SNe. A further possibility is energy injection from a disk around a black hole, resulting from a rapidly rotating massive progenitor. Whatever mechanism may be driving the main supernova light curve, our observations put strong constraints on any progenitor model by requiring a significant mass ejection during the final burning stages before explosion.

Ultimately the supernova ejecta will collide with the shell, which may provide a chance to estimate the composition from the emission. This will occur at a time $R_{\mathrm{in}}/V_{\mathrm{ejecta}}$. From the spectra, we measure a maximum ejecta velocity of $\sim 15,000~~\mathrm{km~s^{-1}}$ (SM), and thus predict that the collision will take place ~ 7 years after the supernova explosion (in the rest frame), or

10 years as observed on Earth. This will result in optical/UV, radio and X-ray radiation, and may in principle be observable depending on the mass of the shell. Especially monitoring the optical flux may be promising in view of the late detection of three SLSN-I (*13, 14*), which may give information about the chemical composition of the shell.

Finally, we consider how unique iPTF16eh is. At least two favorable conditions aligned to make the resonance echo observable: first, the supernova redshift is sufficiently high ($z \gtrsim 0.25$) for Mg II to be easily observable by ground-based optical spectrographs, which typically have limited sensitivity below 3500-4000 Å . In addition, the supernova itself is among the most luminous ever discovered, making it possible to obtain high-quality spectroscopic observations over a long time baseline. Higher-redshift SLSNe that cover the rest-frame UV rarely have late-time spectra available, and thus would not be able to detect a Mg II emission line like the one seen in iPTF16eh. However, the absorption lines from the shell would be readily visible in spectra taken at peak brightness. We have searched through all the spectra of SLSNe from the Pan-STARRS Medium Deep Survey as well as PTF/iPTF, and we do not find evidence of a double Mg II absorption system in any of the spectra with sufficient quality blue spectra to cover these wavelengths (27 total). Given that in the PPI model the time between the first shell ejection and the final core-collapse is a strong function of the He core mass, it is possible that even if such ejections are common, a shell at the distance and velocity separation of iPTF16eh could be rare. The recent detections of late-time Hα emission in three SLSN-I (*13, 14*), interpreted as collision with circumstellar shells located at distances $\sim 10^{16}$ cm, suggest that iPTF16eh is not alone in having a complex circumstellar environment, although the detection of the echo gives unique information about the location, geometry, velocity and mass loss time scale.

Acknowledgments

We are grateful for discussions with Claes-Ingvar Björnsson, Sergei Blinnikov, and Elena Sorokina. The Intermediate Palomar Transient Factory project is a scientific collaboration among the California Institute of Technology, Los Alamos National Laboratory, the University of Wisconsin, Milwaukee, the Oskar Klein Centre, the Weizmann Institute of Science, the TANGO Program of the University System of Taiwan, and the Kavli Institute for the Physics and Mathematics of the Universe. This work was supported by the GROWTH project funded by the National Science Foundation under Grant No 1545949. This research was supported by the Swedish Research Council, the Swedish National Space Board, and the Knut and Alice Wallenberg Foundation. Part of this research was carried out at the Jet Propulsion Laboratory, California Institute of Technology, under a contract with the National Aeronautics and Space Administration. A.G.-Y. is supported by the EU via ERC grant No. 725161, the Quantum Universe I-Core program, the ISF, the BSF Transformative program and by a Kimmel award. PEN acknowledges support from the DOE through DE-FOA-0001088, Analytical Modeling for Extreme-Scale Computing Environments. This research used resources of the National Energy Research Scientific Computing Center, a DOE Office of Science User Facility supported by the Office of Science of the U.S. Department of Energy under Contract No. DE-AC02-05CH11231. Some of the data presented herein were obtained at the W.M. Keck Observatory, which is operated as a scientific partnership among the California Institute of Technology, the University of California and the National Aeronautics and Space Administration. The Observatory was made possible by the generous financial support of the W.M. Keck Foundation. The authors wish to recognize and acknowledge the very significant cultural role and reverence that the summit of Mauna Kea has always had within the indigenous Hawaiian community. We are most fortunate to have the opportunity to conduct observations from this mountain.

Supplementary materials

Materials and Methods

Supplementary Text

Figs. 4 to 7

Tables 1 to 2

References

Materials and Methods

Observational details

iPTF discovery and classification

iPTF16eh was first detected by the intermediate Palomar Transient Factory at coordinates RA=$12^{\mathrm{h}}41^{\mathrm{m}}06.21^{\mathrm{s}}$, Dec=$+32^\circ48'30.9''$ (J2000) on 2015 December 17.5 (UT dates are used throughout this paper), at a magnitude $g = 21.43 \pm 0.23\ \mathrm{mag}$. The photometric coverage on the rise is sparse, as iPTF was conducting a "slow-and-wide" experiment at the time; it was eventually saved as a transient and flagged for follow-up on 2016 February 8. A spectrum taken with SUBARU/Focas on 2016 February 18 revealed a blue continuum with O II absorptions, classifying iPTF16eh as a SLSN-I at an approximate redshift of $z \simeq 0.42$. A subsequent spectrum taken with DBSP on P200 on 2016 February 27 shows narrow Mg II $\lambda\lambda$2796,2803 absorption at $z = 0.413$, though a better S/N spectrum taken with Keck I/LRIS on 2016 March 6 also reveals the presence of a second, weaker Mg II$\lambda\lambda$2796,2803 absorption system at $z = 0.427$. We take this higher-redshift system to be the redshift of the supernova host galaxy.

Photometry

The g-band photometry obtained with the P48 CFH12K camera was processed with the Palomar Transient Factory Image Differencing and Extraction (PTFIDE) pipeline (*23*) to obtain point-spread function (PSF) photometry. In addition, we obtained $Bgri$ photometry with the automated 60-inch telescope at Palomar(P60; (*24*)), including gri data taken with the Spectral Energy Distribution Machine (SEDM; (*25*)), and PSF photometry was performed using `FPipe` (*26*). Additional gri imaging was obtained with the Large Monolithic Imager (LMI) mounted on the 4.3 m Discovery Channel Telescope (DCT) in Happy Jack, AZ. Standard CCD reduction techniques (e.g., bias subtraction, flat fielding) were applied using a custom IRAF[1] pipeline. Individual exposures were astrometrically aligned with respect to references stars from the Sloan Digital Sky Survey (SDSS; (*27*) using SCAMP (*28*). We calculated aperture photometry magnitudes for the transient using an inclusion radius matched to the FWHM of the PSF, and calibrated the images with respect to point sources from SDSS. Additional gr images were also obtained with Low Resolution Imaging Spectrometer (LRIS; (*29*)) on the 10-m Keck I telescope, and were reduced using `LPipe`[2]. Again, aperture photometry was performed and calibrated against point sources in SDSS. Figure 4 shows the observed light curves, and the photometry is listed in Table 1. All photometry has been corrected for Milky Way foreground extinction according to $E(B-V) = 0.015$ (*30*). We assume a standard ΛCDM cosmology with $\Omega_{\mathrm{M}} = 0.27$, $\Omega_{\Lambda} = 0.73$ and $H_0 = 70$ km s^{-1} (*31*).

Spectroscopy

We obtained a total of 12 spectra of iPTF16eh, taken with the Faint Object Camera and Spectrograph (FOCAS; (*32*)) on the 8.2 m Subaru Telescope, the Double Beam Spectrograph (DBSP; (*33*)) on the 200-in Hale telescope at Palomar Observatory, and LRIS on Keck I. LRIS spectra were reduced using LPipe[3], and FOCAS and DBSP spectra were reduced using standard

---

[1] IRAF is distributed by the National Optical Astronomy Observatory, which is operated by the Association of Universities for Research in Astronomy (AURA) under cooperative agreement with the National Science Foundation.

[2] `http://www.astro.caltech.edu/~dperley/programs/lpipe.html`

[3] `http://www.astro.caltech.edu/~dperley/programs/lpipe.html`

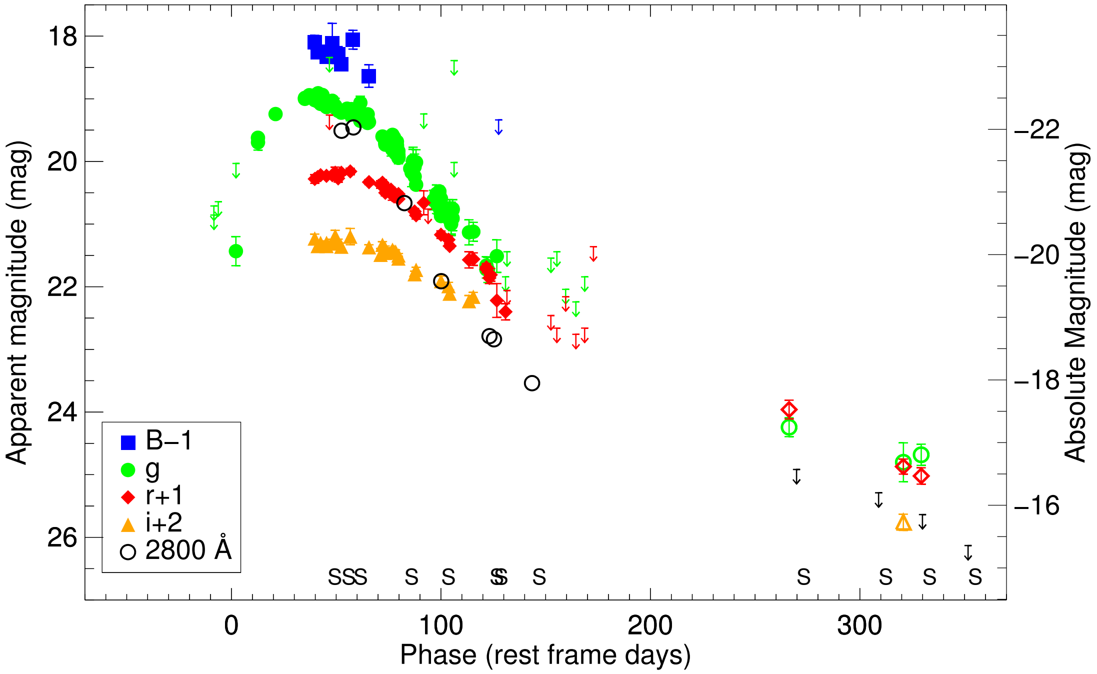

Figure 4 Observed light curve of iPTF16eh. Data is mainly from the P48 and P60 telescopes, and is listed in Table 1. Filters have been offset for clarity as indicated in the legend, and the spectroscopy epochs are marked along the bottom axis. The open symbols after 200 days show unsubtracted photometry, and may have a significant host galaxy contribution. Open circles show the flux at a rest-frame wavelength of 2800 Å, as measured from the continuum flux in the spectra.

pipelines. Table 2 summarizes the spectroscopic observations, and the sequence of spectra is shown in Figure 1. All spectra will be made publicly available through the Weizmann Interactive Supernova Data Repository (WISeREP; (*34*)).

Supernova properties

Light Curve and Energetics

We constrain the explosion date from the g-band light curve, which is the only filter in which we sample the rise. Fitting a second-order polynomial to the observed g-band light curve, we find a best-fit explosion date of 2015 December 14.5 (MJD 57370.5) ± 0.7 day, suggesting that the supernova was discovered just a few days after explosion. Similarly, we find the peak in g-band to be on 2016 February 6.3 (MJD 57424.3) ± 0.8 day. This gives a rest-frame rise time of ~ 38 days. The best-fit peak g-band magnitude is 19.01 mag; given the redshift, observed g-band is close to rest-frame u-band, and we calculate a peak absolute magnitude of $M_u = -22.55$ mag (including a cross-filter K-correction, calculated using SNAKE (*35*)). This makes iPTF16eh one of the most luminous SLSNe observed to date, comparable to e.g. iPTF13ajg (*36*), Gaia16apd (*37*) and PS1-13or (*16*).

From peak light onwards we have multi-filter data, which we can use to measure other supernova properties such as the temperature evolution and pseudo-bolometric flux. Fitting a blackbody, we find that iPTF16eh had a color temperature of $\sim 16,000$ K near peak, and declined at a rate of approximately $110\ \mathrm{K\ day}^{-1}$ post-peak. We follow the procedure outlined in (*16*) to construct a pseudo-bolometric light curve, and find a lower limit on the peak bolometric luminosity of $2.7 \times 10^{44}\ \mathrm{erg\,s}^{-1}$, and a minimum radiated energy of 1.3×10^{51} erg. These are, again, at the high end of what has been observed for SLSNe, though within the observed distribution (*16, 17*). The light curve timescales are similar to other "slowly-evolving" SLSNe such as PTF12dam and PS1-11ap (*38*). The blackbody temperatures and radii, as well as our

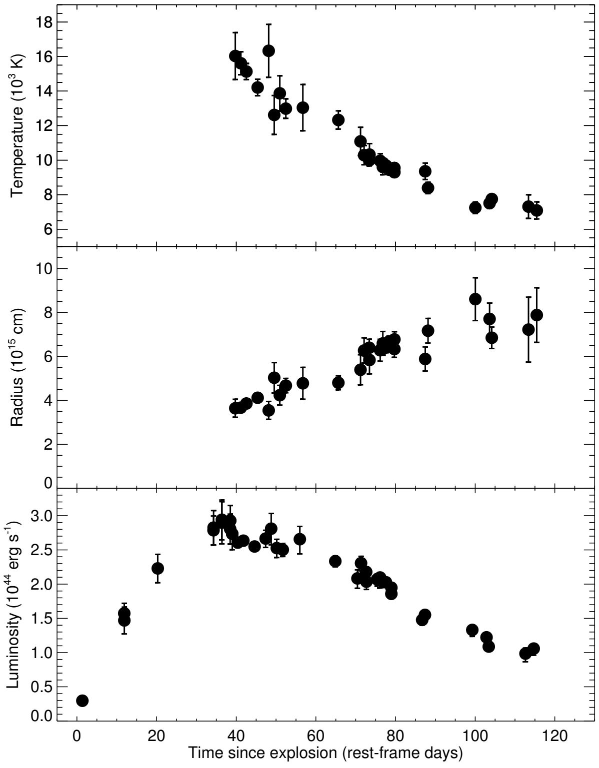

Figure 5 Evolution of the blackbody temperature (top), blackbody radius (middle), and pseudo-bolometric luminosity (bottom). As we do not have multiband data on the rise of the light curve, the points on the rise are calculated scaling from the g-band light curve and assuming a constant bolometric correction.

pseudo-bolometric light curve (assuming a constant bolometric correction on the rise) are shown in Figure 5

Spectroscopic Properties

The overall spectroscopic evolution of iPTF16eh is also very similar to other well-studied H-poor SLSNe – Fig. 6 shows comparisons to iPTF13ajg (*36*), PTF12dam (*39*) and SN 2015bn (*40*) at similar epochs. Near peak, the spectrum shows a blue continuum with weak O II features in the optical, with a broad, stronger UV feature bluewards of 2800 Å that is usually interpreted as a blend of Mg II and C II (*41*). As the ejecta cool, the spectrum evolves to show features typical of stripped-envelope SNe, mainly from Fe II, Ca II, Si II and Mg II. As can be seen from the comparisons with the other SLSNe, apart from the intermediate-width Mg II emission line at late epochs discussed in the main text, iPTF16eh does not display any unusual spectroscopic features.

Determining the ejecta velocity from SLSN spectra can be challenging, as the lines available at peak light are different from those most often used and studied in other stripped-envelope SNe (e.g., Fe IIλ5169 or Si IIλ6355). From the "W"-shaped O II feature around 4300 Å in our earliest spectrum (Fig. 1), we derive an ejecta velocity of $8,500\ \mathrm{km\,s^{-1}}$. On the other hand, if we assume that the broad UV feature at ~ 2620 Å is due to Mg II, we would derive a much higher velocity of $\sim 20,000\ \mathrm{km\,s^{-1}}$. This discrepancy could be due to the Mg II line forming further out in the ejecta than the O II line, or, more likely, that the feature we see is a blend of multiple ions. The evolution of the blackbody radius (Fig. 5) suggests an expansion velocity of $\sim 8,000\ \mathrm{km\,s^{-1}}$, consistent with the measurement from the O II lines. The blue edge of the same absorption line suggests there is material moving at speeds up to at least $15,000\ \mathrm{km\,s^{-1}}$.

Host Galaxy

No host galaxy is detected at the location of iPTF16eh in either SDSS or Pan-STARRS1 3π pre-explosion images, and our latest photometry measure a combined supernova and host brightness $m_g \simeq 24.7 \pm 0.2$ mag. This places an upper limit on the host absolute magnitude of $M_g \gtrsim -16.8$ mag, suggesting that the host of iPTF16eh is a faint dwarf galaxy. Such an environment is not unusual for SLSN-I, which show a strong preference for low-mass, low-metallicity host galaxies (*42, 43*).

We measure the equivalent width of the Mg II lines from the host galaxy ISM to be about 1.6 ± 0.4 Å, with the main uncertainty coming from the uncertainty in the continuum level

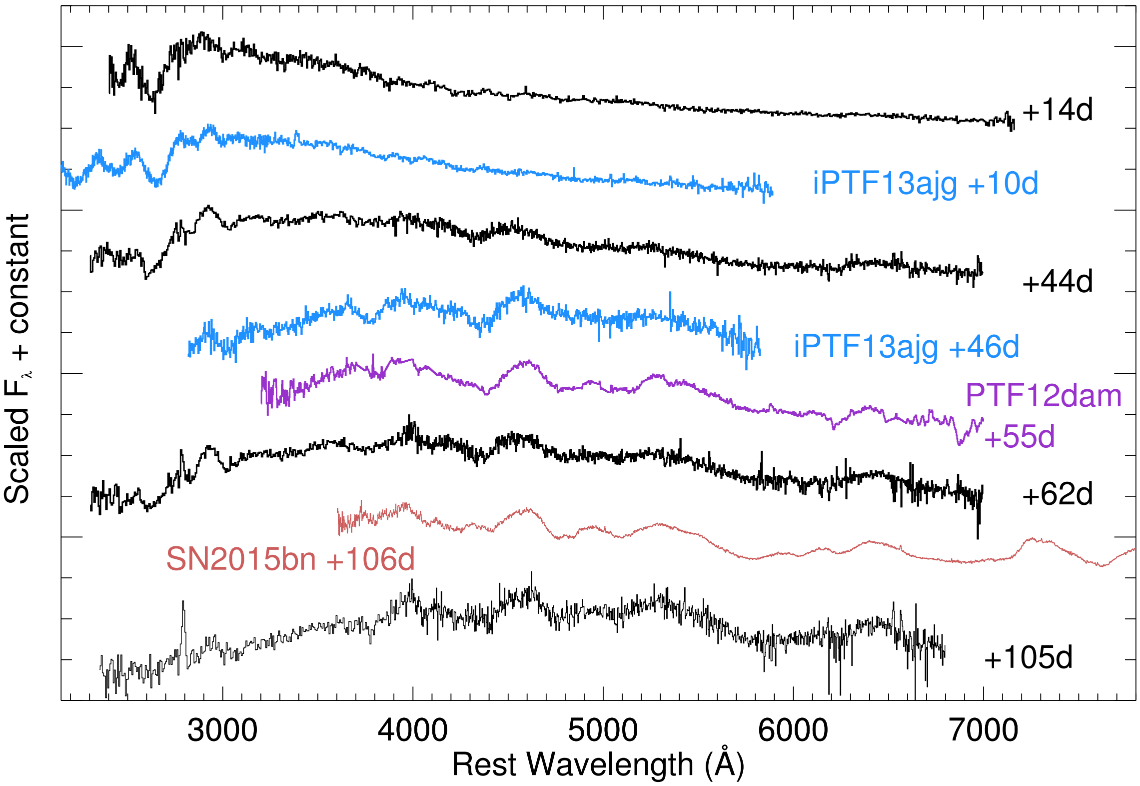

Figure 6 Spectra of iPTF16eh compared to the well-studied SLSNe PTF12dam (*39*), iPTF13ajg (*36*), and SN 2015bn (*40*). To facilitate comparisons, supernova phases are shown relative to peak light (MJD 57424.3 in the case of iPTF16eh).

(from both measurement uncertainty and the features in the supernova spectrum). This value is consistent with the distribution for SLSN-I host galaxies measured in (*36*), and again suggests that the host galaxy of iPTF16eh is not unusual in the context of SLSN-I host galaxies.

Modeling the Scattered Shell Emission

Basic Echo Model

We calculate synthetic spectra using a Monte Carlo code, which calculates the scattering by the shell, assuming optically thick lines and isotropic scattering in the rest frame of the shell. The basic geometry is shown in Fig. 7, along with light echo parabolas showing which part of the shell is contributing to the observed emission at three different epochs. The outer parabola corresponds to the time of supernova shock breakout, while the inner parabola corresponds to the fading away of the supernova light. As illustrated, the observed emission line profile from the shell relates to both the input light curve and the shell thickness (and more generally, the velocity profile).

The number of photons emitted from the shell at a given time is proportional to the continuum flux from the supernova photosphere. Therefore, the form of the light curve between $\sim 2765 - 2834$ Å (for an expansion velocity $\sim 3300 \text{ km s}^{-1}$) is important. We determine the continuum in this range from the available spectra, shown as black points in Fig. 4. Unfortunately, we lack spectra on the rise of the light curve, and have to make assumptions about the flux in this wavelength range prior to the first spectrum.

As a simple parameterisation we use a generalized Gaussian distribution given by

$$F_\lambda(2800\text{Å}) = C\frac{e^{-y^2/2}}{\alpha - \kappa(t_{\text{day}} - \zeta)} \tag{1}$$

where $y = -\ln[1 - \kappa(t_{\text{day}} - \zeta)/\alpha]/\kappa$. As our standard model we use $\zeta = 41$ days, $\alpha = 23$ days and the shape parameter $\kappa = -0.28$, which gives a good fit to the continuum light curve at 2800 Å in Fig. 4 after the peak. At earlier epochs we use the form of the uvw1 light curve

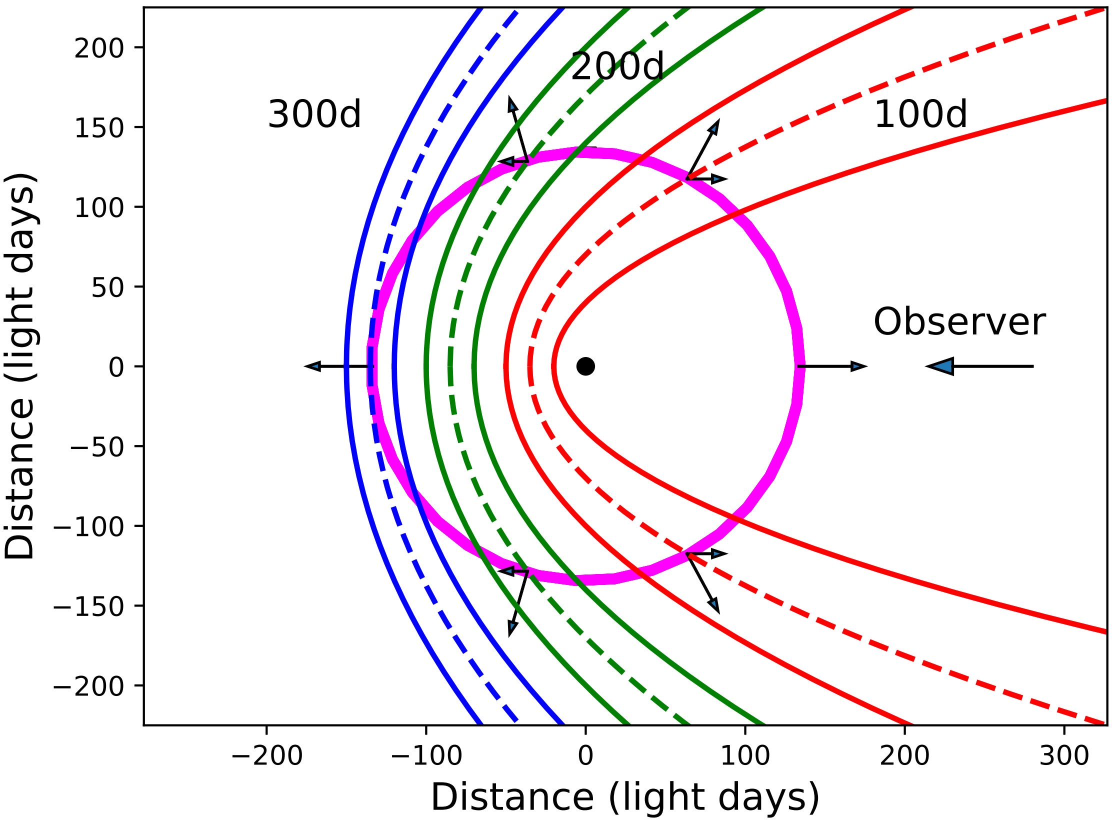

Figure 7 Approximate geometry of the shell and light echo parabolas, corresponding to three different observed epochs, 100, 200 and 300 days after explosion. Dimensions are in light days. The outer parabola corresponds to the shock breakout, the inner to an approximate fading and the dashed to the peak luminosity. The radial and horizontal arrows correspond to the expansion velocity of the ring, $\sim 3300\,\mathrm{km\,s^{-1}}$, and the line of sight velocity for the peak of the light curve, respectively. The spatial scale of the axes is in light days.

calculated for PTF12dam in (*19*), stretched by a factor 1.15. This model gives a good fit to the observed g-band light curve of iPTF16eh and also the observed part of the 2800 Å light curve, and is therefore a reasonable assumption for the rising part of the latter. The above parameters in Eq. (1) gives a good fit to this. However, the early flux at 2800 Å could be different and for this reason we discuss variations of this below.

We emit the photons in random directions from the photosphere in the interval 2760 - 2840 Å. The doublet nature of the lines complicates the radiative transfer, since a photon scattered in the $\lambda 2795.5$ line may be further scattered by the $\lambda 2802.7$ line. Only photons below 2802.7 Å will be scattered, while those above will escape directly or be absorbed by the photosphere. The time for each photon from its emission until it arrives at a common surface relative to the line of sight is calculated. For a single line and homologous expansion a photon emitted at $t_{\rm emiss}$ from a radius r_1 at a cosine angle μ_1 will arrive at

$$t = t_{\rm emiss} + (R_{\rm out} x - r_2 \mu_2)/c \tag{2}$$

Here μ_2 is the cosine angle relative to the radial direction of the scattered photon at the radius of scattering r_2, given by

$$r_2 = [r_1^2 + (x R_{\rm out})^2 + 2 x R_{\rm out} r_1 \mu_1]^{1/2} \tag{3}$$

and the dimensionless frequency shift is

$$x = \frac{\nu - \nu_0}{\nu_0} \frac{c}{V_{\rm max}}. \tag{4}$$

Equation (3) describes a spherical surface with radius $x R_{\rm out}$ centered at r_1. For the constant velocity case similar equations are obtained, although somewhat more complicated. We assume isotropic scattering in the rest frame of the gas.

The thickness of the shell influences both the shape of the line profile and the flux relative to the nearby continuum, being roughly proportional to the cross sectional area of the shell,

$\pi(R_{\rm out}^2 - R_{\rm in}^2)$ (Fig. 7). The fraction scattered is then $\sim \Delta R/R$, where ΔR is the thickness of the shell. From the observed ratio of the luminosity of the continuum emission at 2800 Å and the luminosity of the emission at the late epochs we find that the range $R_{\rm in} = 130$ light days and $R_{\rm out} = 137$ light days gives a good agreement with the observations. This is only weakly dependent on the velocity law used.

If it had not been for the importance of the large light travel time compared to the evolutionary time scale of the photospheric emission this would have resulted in an ordinary P-Cygni line, with nearly zero equivalent width.

Optical Depth of Mg II

For the resonance scattering scenario to work the Mg II lines have to be optically thick. Assuming a homologous expansion and using the derived parameters for the volume of the shell from the main section, the optical depth of the Mg II line can be estimated as

$$\tau = \frac{A_{21}\lambda^3 n_1 t}{8\pi g_1} \approx 3.2 \times 10^6 X({\rm MgII}) \left(\frac{M_{\rm shell}}{M_\odot}\right) \ , \tag{5}$$

where A_{21} is the transition rate, λ the wavelength, g_1 the statistical weight of the lower state (equal to 2), n_1 the number density in the ground state and $X(\text{Mg II})$ the Mg II ionic abundance. The time t is taken as the time since ejection discussed earlier, ~ 35 years. The solar Mg abundance is $\sim 4 \times 10^{-5}$ by number. For a shell with a mass $\gtrsim 1\ M_\odot$ (as we argue in the main text) the optical depth can therefore be large even if the abundance is less than solar, as long as most of the Mg is in Mg II. This is likely to be the case, unless there is a very strong flux above ~ 15 eV.

Model Variations

In the main section of the paper we show the evolution of the line profiles for the 'standard' model with $R_{\rm in} = 130$ light days and $R_{\rm out} = 137$ light days and the parametrization of Eq. (1)

of the continuum flux. To illustrate the effects of the doublet scattering we show in the upper right panel in Fig. 8 a model with the same parameters, but for only a single line at 2800 Å. Compared to the single line simulation one notes the double peak nature of the line profiles. Because of the scattering from the blue to the red component the line profile is, however, not a simple sum of the two components. The roughly double intensity of the line for the doublet is a result of the twice as large continuum covering by the doublet.

The influence of the unobserved continuum light curve before the peak is also shown in Fig. 8 for a model where we have assumed a constant flux before the peak and after that the observed decline. As for the case of the burst in the main section, the line profile reflects this as a plateau on the long wavelength side of the line. Finally we show the effect of different shell parameters, $R_{\rm in} = 150$ light days, $R_{\rm out} = 160$ light days for the standard light curve. Compared to the standard case this results in narrower line profiles, but, as expected, a slower velocity evolution.

Supplementary Text

Ruling out alternative explanations of the narrow Mg II lines

We can rule out that the Mg II emission lines are originating in the SN ejecta due to a peculiar chemical composition, since this would require an almost complete abundance of Mg. Nuclear burning zones with a high abundance of Mg nearly always have even higher abundance of O and Ne. One would therefore expect strong emission lines of O I-III, as well as Ne III-V and Mg I from the shell.

Direct interaction with a CS shell, as in SN 2001em (*44*) and SN 2014C (*45–48*), can be ruled out from the time scale and line shifts, as well as the absence of He and metal lines, which would dominate the cooling for abundances typical of H-, He- or O-rich zones. A further argument is based on the observed line shifts with timeFor an expansion velocity $V_{\rm exp}$ the shell

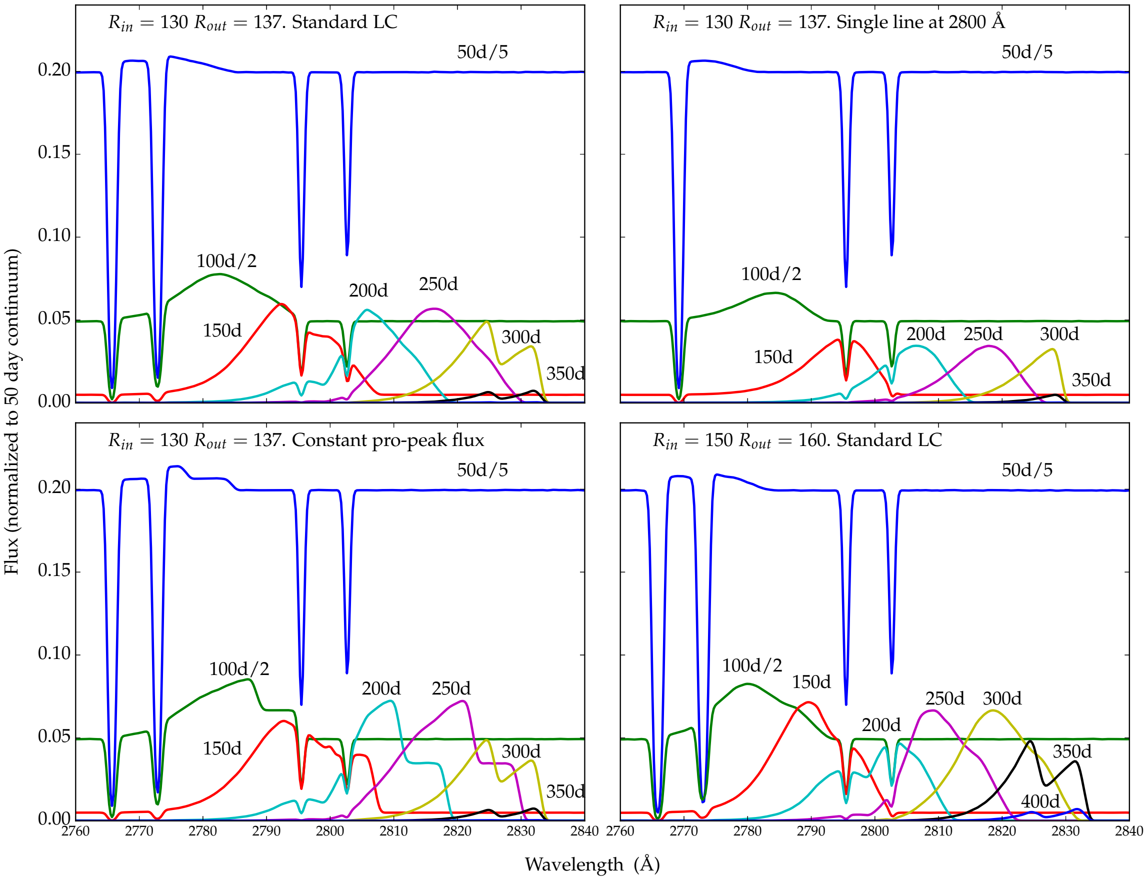

Figure 8 *Upper left:* Standard values for the light curve and shell, $R_{\text{in}} = 130$ light days, $R_{\text{in}} = 137$ light days. *Upper right:* Same parameters, but with only a single line at a rest wavelength 2800 Å. Note the double-peaked line profiles, the broader lines, as well as the nearly double intensity in the doublet case. *Lower left:* Same shell parameters, but constant continuum flux before the peak. Note the flat red plateau in the line profile. *Lower right:* Effect of changing the parameters of the shell to $R_{\text{in}} = 150$ light days, $R_{\text{in}} = 160$ light days. Standard light curve. Note the slower evolution in wavelength and narrower line profiles. No smoothing due to the instrumental resolution has been applied too these simulations.

has to be at $t_{\rm shell} V_{\rm exp}$, where $t_{\rm shell}$ is the first detection of the lines. To be conservative $t_{\rm shell} \sim 100$ days. Even for an extreme velocity of $0.2c$ the shell would have to be at $\lesssim 5 \times 10^{16}$ cm. Light travelling time effects would then be only of order $V_{\rm exp}/c$, and would not be important for explaining the drifting velocity. A decreasing velocity of the shock from negative to positive would also be extremely difficult to understand.

Based on the shell velocity, an echo from the wind of a Wolf-Rayet star could be a possibility. This can, however, be refuted on several grounds. First, the state of ionization of a WR wind is considerable higher, with typical ions being C IV, N V and O VI, but with no absorption lines from Mg II. If it was instead coming from the interaction region between the WR wind and the slow material from a previous RSG or LBV stage the velocity would be of the order of hundreds of $\rm km\,s^{-1}$ and not $\sim 3300\ \rm km\,s^{-1}$.

Constraints on the shell mass and composition

Lack of other resonance lines

The Mg II doublet is one of the few strong resonance lines of the abundant elements in the observed part of the spectrum. The other possible resonance lines are the Ca II $\lambda\lambda 3968.5, 4226.7$ H and K lines, the Na I D $\lambda\lambda 5890.0, 5895.9$ doublet and the K I $\lambda\lambda 7664.9, 7699.0$ doublet. In addition, there are weaker lines from Fe II and Ti II.

Both Na I and K I are easily ionized out to very large distances by the radiation from the SN due to their low ionization potentials 5.14 and 4.34 eV, respectively. With regard to the Ca II lines the solar Ca abundance is only $\sim 5\%$ of the Mg abundance, while the atomic line parameters, like the transition rate and excitation energy, are comparable. In addition, the ionization potential of Ca II is only 11.82 eV, below the H I and O I ionization edges, and therefore subject to a strong ionizing flux from the SN. Mg II with an ionization potential of 15.03 eV is more resistant to this. Given the hot SN continuum, it is therefore not surprising that no Ca II absorption lines are seen from the shell.

Constraint on the Hα emission from the shell

If the progenitor had some of the H envelope left before the first ejection this would temper the velocity and also change the time between the first pulse and core collapse. Unfortunately, we do not have any strong constraints on the composition of the shell from observations. An upper limit to the H mass can be obtained from the Hα luminosity, $L_{H\alpha}$. Given the high radiation temperature at the first observations (Fig. 5) we assume that the shell is fully ionized shell and dominated by hydrogen. Then

$$L_{H\alpha} \approx 3.5{\times}10^{36} f^{-1} \left(\frac{T_{\rm e}}{10^4{\rm K}}\right)^{-0.94} \left(\frac{M_{\rm shell}}{M_\odot}\right)^{2} \left(\frac{R_{\rm shell}}{5\times10^{17}{\rm cm}}\right)^{-3} \left(\frac{\Delta R_{\rm shell}/R_{\rm shell}}{0.1}\right)^{-1} \ {\rm erg\,s^{-1}}, \tag{6}$$

where f is the filling factor of the shell. For $R_{\rm shell} \approx 3.5\times10^{17}$ cm and $\Delta R_{\rm shell}/R_{\rm shell} \approx 0.06$ one obtains $L_{H\alpha} \approx 9.6\times10^{36}(M_{\rm shell}/\ M_\odot)f^{-1}$ erg s^{-1}. To estimate an upper limit to the Hα flux we take the February 2017 spectrum, which has the best S/N of the spectra where the peak of the line is well separated from the Hα from the host galaxy (using the velocity shift from the Mg II line). Using also the same line profile as for the Mg II line at this epoch, we find a flux of 1.2×10^{-17} erg s^{-1}cm^{-2}, corresponding to $L_{H\alpha} \lesssim 8.1\times10^{39}$ erg s^{-1} for standard cosmological parameters. Any emission from a hydrogen dominated shell with $M \lesssim 28f\ M_\odot$ would therefore be difficult to detect, unless the filling factor is small. This is mainly a result of the large distance to the shell and therefore low density.

Geometry of the shell

As argued in the main text, the fact that the shell is seen in both emission and absorption at very similar velocities, as well as the smooth velocity evolution (Fig. 2) argues for the shell being symmetric. Further information on the geometry comes from comparing the absorbed and re-emitted flux, which constrains the covering fraction.

From the scattered emission measured by the time integrated absorbed flux in the two doublet components at 2767 and 2775 Å one can estimate the total number of of photons scattered by the shell. For a spherical shell with a complete covering factor this should be equal to the total number of emitted photons in the emission component, corrected for the negligible absorption by the photosphere. To estimate the total scattered flux we have measured the equivalent width of the blue component, which is not affected by the scattered emission. We determine the continuum level from the average flux on the blue side of the lines between 2750 to 2763 Å. From the spectra with the highest signal to noise in the continuum (days 52, 28, 82, 100, 125) we find an equivalent width of 2.0 Å in the rest frame of the SN. Using the continuum light curve in Eq. (1) with $C = 4.5 \times 10^{-15}\ \ \mathrm{erg\ s^{-1} cm^{-2}\ \AA^{-1}}$ and multiplying this with 2.0 Å we can estimate the total absorbed flux in the blue 2795.5 Å component to $\sim 1.8 \times 10^{-9}\ \mathrm{erg\ cm^{-2}}$. Assuming that the red 2802.7 Å component contributes the same we arrive at $\sim 3.6 \times 10^{-9}\ \mathrm{erg\ cm^{-2}}$.

To estimate the total flux in the emission component we assume from Fig. 2 a constant flux of $\sim 1.75 \times 10^{-16}\ \mathrm{erg\ cm^{-2}\ s^{-1}}$ during 250 days, taking the rise and decline of the flux into account. We then find a total flux of $\sim 4.5 \times 10^{-9}\ \mathrm{erg\ cm^{-2}}$ for the emission component. Given the uncertainties in both the absorbed flux (lack of spectra in the rising part of the light curve and the general continuum level for the equivalent width estimate) and also in the the emitted flux (including the lack of observations in the middle part of the light curve), these two values are consistent within the errors. For an incomplete covering factor, e.g. a ring or torus, one would expect the emission flux to be much less than the scattered flux in the absorptions. We therefore conclude that the geometry is consistent with a spherical shell.

Circumstellar emission in other related SNe

While iPTF16eh is the first supernova to show a resonance echo, there are several examples of supernovae where the presence of late-time mass loss is inferred. For example, the Type I SLSNe iPTF13ehe (*13*), iPTF15esb and iPTF16bad (*14*) all show broad Hα emission at late epochs, interpreted as emission from a shocked shell excited by the expanding ejecta. The inferred radius for the shells in these cases is a few times 10^{16} cm, about an order of magnitude further in than for iPTF16eh.

We note that the velocities inferred for the shock from the Hα profiles in these objects ($\sim 4000\ \ \mathrm{km\ s^{-1}}$ in the case of iPTF13ehe) would be extreme, unless the CSM is very dense. In light of iPTF16eh, an alternative could be that the excitation is instead coming from ionizing radiation originating in the supernova explosion. This could either be from an early burst connected to the shock breakout or from the later emission from the photosphere if this is hot enough. The observed Hα would then come from the recombination of the ionized shell. Except for the much higher velocity, this is similar to the mechanism which excited the ring of SN 1987A (*49*). This has the important implication that the distance to the Hα emitting material could be much larger, and that the velocity of the Hα line would be characteristic of the shell, in the same way as discussed here for iPTF16eh. For the same geometric parameters as for iPTF16eh this would require a mass $\gtrsim 10\ M_\odot$ for a filling factor $\gtrsim 0.1$.

There are other SNe showing dense shells of CS gas. The condition to observe an echo or not is that $\tau \ll R_{\rm shell}/c$ where τ is the characteristic duration of the exciting radiation. This was the case of SN 1987A, where the exciting radiation of the circumstellar ring was the shock breakout radiation which had a time scale of minutes, while the ring is at a distance of ~ 200 light days, and an echo was clearly observed. In this case the emission from the ring was seen mainly as UV lines (*50*). Because the expansion velocity of the ring was only $\sim 10\ \mathrm{km\ s^{-1}}$, only a marginal shift in wavelength with time was seen. Moreover, the recombination time of the gas was long, which smoothed the evolution (*49*). Except for the N V $\lambda\lambda 1238, 1242$ lines, the excitation was mainly by collisions in the hot gas.

Two other related cases are the stripped SNe 2001em (*44*) and SN 2014C (*45–48*). For the latter, radio, optical, and X-ray observations have revealed a shell of hydrogen rich gas at $\sim 6 \times 10^{16}$ cm with a mass of $\sim 1\ M_{\odot}$. The analysis of SN 2001em yielded a similar radius for the shell, with a somewhat higher mass, $2 - 3\ M_{\odot}$ (*44*). The light travel time is for these shells ~ 20 days, which is shorter than the width of the light curve. Echoes, such as the ones we see in iPTF16eh, are therefore not likely to be important for these.

Constraints on the progenitor

As discussed in the main text, we believe that the most likely explanation for the shell is a PPI ejection before the final explosion, although an LBV related eruption, similar to that of Eta Carinae, cannot be excluded. However, as discussed in (*12*), an LBV may also be a result of PPI ejections. Here, we compare the inferred properties of iPTF16eh more closely to PPI models, to see what constraints can be obtained for the progenitor star.

The observations give a shell velocity, $\sim 3300\ \mathrm{km\ s^{-1}}$, with a radius, $\sim 3.5 \times 10^{17}$ cm, implying a time scale of ~ 32 years, if undecelerated. From the limit of the Hα luminosity we derived a weak limit on the hydrogen mass of $M \lesssim 28 f\ M_{\odot}$. It could therefore be dominated by either hydrogen or helium. The shell is likely to be close to spherical with a large covering factor.

For the PPISNe the main parameters for the time between the first shell ejection and the subsequent ones and the final core collapse is the mass of the He core, increasing rapidly above $\sim 50\ M_{\odot}$ (Table 1 in (*12*)). For a bare He core without rotation a time scale of ~ 32 years corresponds to a He core mass of $\sim 54\ M_{\odot}$.

The presence of a massive H shell leads to a somewhat smaller He core mass for the same duration between the first ejection and final explosion, $\sim 51 - 53\ M_{\odot}$ (e.g., model T115B with a time scale of 39 years in Table 2 in (*12*)). The mass of the H envelope depends strongly on the mass lost in the preceding evolution. For a very massive envelope, $\gtrsim 10\ M_{\odot}$, the main difference compared to the bare He core is that the velocity of the ejected mass is much lower, $\lesssim 1000\ \mathrm{km\ s^{-1}}$. For lower masses the velocity increases. Based on the observed velocity we therefore favor the bare He core models or models with a low mass H envelope, $\lesssim 10\ M_{\odot}$. Because the Mg abundance in the He core is not very different from that of the H envelope, the required mass to make the Mg II lines optically thick (Eq. 5) is independent of the composition as long as it is does not contain processed magnesium.

An example of a model with a low mass H envelope that gives about the right shell ejection properties is B115-5 in Table 4 of (*12*). This was (by construction) a blue supergiant (or LBV, whose properties would have been similar) with a hydrogen envelope mass of $4.9\ M_{\odot}$ (though the hydrogen mass fraction in this envelope was only 0.2). The first two pulses ejected $6.7\ M_{\odot}$ including all this envelope. The total kinetic energy for that ejection was 6.6×10^{50} erg. 5.2 years later two additional pulses separated by about 20 days ejected an additional $4.0\ M_{\odot}$ with a total kinetic energy of 3.5×10^{50} erg. This matter was mostly He with some new C, O, Ne, and Mg. About 10 days later the remaining $45.9\ M_{\odot}$ core collapsed, probably to a black hole.

At the time of the final outburst the former ejected shell was moving at $3100\ \mathrm{km\ s^{-1}}$ at a radius of about 5×10^{16} cm. This is too small for iPTF16eh because the envelope was only ejected 5 years before the final outburst. The delay time is, however, very sensitive to the mass of the core and to some extent the mass of the H envelope. A $20\ M_{\odot}$ envelope on the same model gave a delay of 14 years, but then the shell would have moved much slower. A combination of a somewhat heavier star with a hydrogen envelope mass of $\sim 5\ M_{\odot}$ is likely to result in a delay of ~ 30 years.

In summary, a PPISN can eject several solar masses of material years to decades before the final explosion. For a 30 year delay, the main sequence mass is close to $115\ M_\odot$ and the He core mass close to $52\ M_\odot$. Given the severe energy restrictions on the PPISN model the mass of the fossil shell, possibly H-rich, can be no more than about $10\ M_\odot$.

Powering the supernova light curve

While the above models agree well with the velocity and time scale of the observed shell, the most problematic aspect is that the SNe predicted for these models are not superluminous. The light curve of the final explosion for model B115-5 lacks the duration and high luminosity of iPTF16eh. In general, it is hard to get it much brighter without more mass, meaning lower ejection speeds, in a pure PPISN model. Further, we find a total radiated energy of $\sim 1.3 \times 10^{51}$ erg for iPTF16eh, while the maximum energy of the pure PPISN models in (*12*) is $\sim 5 \times 10^{50}$ erg. Additional energy input may therefore be needed and there are several possibilities for this, all, however, somewhat speculative.

A pure magnetar model could provide the extra energy. This would correspond to the 'standard' magnetar model for a SLSN-I (*3*). There is, however, for these no natural explanation for the shell formation. An LBV eruption connected to the last burning stages may be a possibility (*11*), although the cause is not well understood.

A second possibility is that a high mass PPISN also makes a magnetar. The problem is here the high mass of the Fe core for these massive stars, which tends to result in a collapse to a black hole rather than a neutron star. A possible scenario is, however, that the PPISN first ejects the observed shell and at the core collapse a milli-second magnetar forms from the 2.1 $M_\odot$ Fe core (as in model B115-5). The magnetar is born about 10 days after the last shell ejection. Initially the field has to be very strong ($\gtrsim 10^{15}$ G) injecting $\sim 10^{52}$ erg to blow up the star. To power the light curve over a longer period the magnetic field has to decay to $\lesssim 10^{14}$ G before the neutron star radiates all its energy. This obviously needs a high degree of fine tuning.

In the final scenario a black hole of about 40 $M_\odot$ is born, but matter at its outer boundary has enough rotation and magnetic field to form a disk and make jets. This takes more rotation than the above options and may be difficult to achieve if there has been a lot of mass loss or the star has been a giant. But if a disk forms $1\ M_\odot$ accreted mass could give $\sim\ 10^{53}$ erg, which might come out as a broad jet. Interaction with matter at $10^{14} - 10^{15}$ cm from the mass ejections a week before may then lead to a bright enough light curve. The event would, however, probably be asymmetric.

Table 1. iPTF16eh Photometry

MJD (days)	Rest-frame Phase (days)	Filter	AB Mag	Instrument
57358.53	-8.39	g	> 20.71	P48
57358.56	-8.37	g	> 20.86	P48
57361.54	-6.28	g	> 20.64	P48
57373.54	2.13	g	21.43 ± 0.23	P48
57373.57	2.15	g	> 20.03	P48
57388.55	12.65	g	19.62 ± 0.07	P48
57388.58	12.67	g	19.70 ± 0.12	P48
57400.55	21.06	g	19.24 ± 0.07	P48
57420.53	35.05	g	19.00 ± 0.03	P48
57420.56	35.08	g	18.99 ± 0.06	P48
57423.53	37.15	g	18.94 ± 0.08	P48
57423.56	37.18	g	18.96 ± 0.09	P48
57426.50	39.24	g	18.99 ± 0.04	P48
57426.54	39.26	g	18.95 ± 0.03	P48
57427.25	39.76	B	19.10 ± 0.11	P60+GRBcam
57427.25	39.76	g	19.02 ± 0.05	P60+GRBcam
57427.25	39.76	r	19.28 ± 0.07	P60+GRBcam
57427.25	39.76	i	19.23 ± 0.07	P60+GRBcam
57429.24	41.16	B	19.26 ± 0.05	P60+GRBcam
57429.24	41.16	g	19.04 ± 0.03	P60+GRBcam
57429.25	41.16	r	19.25 ± 0.03	P60+GRBcam
57429.25	41.16	i	19.35 ± 0.04	P60+GRBcam
57429.52	41.35	g	19.03 ± 0.04	P48
57429.55	41.37	g	18.91 ± 0.03	P48
57431.24	42.55	B	19.25 ± 0.05	P60+GRBcam
57431.24	42.56	g	19.08 ± 0.02	P60+GRBcam
57431.24	42.56	r	19.22 ± 0.02	P60+GRBcam
57431.24	42.56	i	19.30 ± 0.03	P60+GRBcam
57432.47	43.42	g	19.01 ± 0.03	P48
57432.51	43.44	g	18.94 ± 0.04	P48
57435.26	45.37	g	19.13 ± 0.03	P60+GRBcam
57435.26	45.37	r	19.23 ± 0.03	P60+GRBcam
57435.26	45.37	i	19.35 ± 0.03	P60+GRBcam
57435.29	45.40	B	19.33 ± 0.05	P60+GRBcam
57435.30	45.40	i	19.30 ± 0.03	P60+GRBcam
57437.22	46.75	g	> 18.34	P60+GRBcam
57437.22	46.75	r	> 18.26	P60+GRBcam
57439.21	48.14	B	19.12 ± 0.32	P60+GRBcam
57439.22	48.14	g	19.03 ± 0.06	P60+GRBcam
57439.22	48.15	r	19.22 ± 0.05	P60+GRBcam
57439.22	48.15	i	19.30 ± 0.06	P60+GRBcam
57441.21	49.54	B	> 19.14	P60+GRBcam
57441.21	49.54	g	19.11 ± 0.12	P60+GRBcam
57441.21	49.54	r	19.18 ± 0.09	P60+GRBcam
57441.21	49.54	i	19.19 ± 0.09	P60+GRBcam
57443.20	50.94	B	19.29 ± 0.12	P60+GRBcam
57443.21	50.94	g	19.19 ± 0.06	P60+GRBcam
57443.21	50.94	r	19.27 ± 0.06	P60+GRBcam
57443.21	50.94	i	19.31 ± 0.07	P60+GRBcam
57445.36	52.45	B	19.45 ± 0.08	P60+GRBcam
57445.36	52.45	g	19.22 ± 0.03	P60+GRBcam
57445.36	52.45	r	19.18 ± 0.04	P60+GRBcam

Table 1 (cont'd)

MJD (days)	Rest-frame Phase (days)	Filter	AB Mag	Instrument
57445.37	52.45	i	19.36 ± 0.06	P60+GRBcam
57449.28	55.20	g	19.20 ± 0.06	P48
57449.32	55.22	g	19.16 ± 0.05	P48
57451.47	56.73	r	19.16 ± 0.05	P60+SEDM
57451.48	56.73	i	19.20 ± 0.13	P60+SEDM
57451.48	56.74	g	19.25 ± 0.10	P60+SEDM
57452.28	57.30	g	19.17 ± 0.05	P48
57452.31	57.32	g	19.23 ± 0.08	P48
57453.32	58.03	u	20.52 ± 0.25	Swift+UVOT
57453.32	58.03	uvm2	22.64 ± 0.29	Swift+UVOT
57453.32	58.03	uvw2	> 22.92	Swift+UVOT
57453.32	58.03	uvw1	21.89 ± 0.30	Swift+UVOT
57453.32	58.03	B	19.06 ± 0.15	Swift+UVOT
57453.32	58.03	V	18.93 ± 0.25	Swift+UVOT
57456.28	60.10	g	19.21 ± 0.06	P48
57456.32	60.13	g	19.21 ± 0.06	P48
57456.35	60.15	g	19.17 ± 0.04	P48
57457.28	60.80	g	19.22 ± 0.09	P48
57457.32	60.83	g	19.18 ± 0.05	P48
57457.35	60.85	g	19.24 ± 0.06	P48
57458.28	61.50	g	19.25 ± 0.05	P48
57458.32	61.53	g	19.35 ± 0.08	P48
57458.35	61.55	g	19.06 ± 0.11	P48
57462.35	64.35	g	19.33 ± 0.06	P48
57463.29	65.01	g	19.39 ± 0.06	P48
57463.32	65.03	g	19.25 ± 0.05	P48
57463.35	65.05	g	19.32 ± 0.06	P48
57464.18	65.63	B	19.64 ± 0.18	P60+GRBcam
57464.20	65.65	g	19.37 ± 0.04	P60+GRBcam
57464.20	65.65	r	19.33 ± 0.04	P60+GRBcam
57464.20	65.65	i	19.37 ± 0.04	P60+GRBcam
57472.13	71.21	r	19.37 ± 0.06	P60+GRBcam
57472.13	71.21	i	19.49 ± 0.10	P60+GRBcam
57473.41	72.10	r	19.34 ± 0.05	P60+SEDM
57473.41	72.10	i	19.33 ± 0.05	P60+SEDM
57473.42	72.11	g	19.60 ± 0.07	P60+SEDM
57475.27	73.40	r	19.40 ± 0.03	P60+SEDM
57475.27	73.40	i	19.39 ± 0.04	P60+SEDM
57475.27	73.40	g	19.70 ± 0.04	P60+SEDM
57475.35	73.46	r	19.50 ± 0.05	P60+SEDM
57475.35	73.46	i	19.46 ± 0.07	P60+SEDM
57475.35	73.46	g	19.73 ± 0.07	P60+SEDM
57479.18	76.14	r	19.45 ± 0.04	P60+SEDM
57479.18	76.14	i	19.45 ± 0.07	P60+SEDM
57479.18	76.14	g	19.75 ± 0.04	P60+SEDM
57479.23	76.18	g	19.68 ± 0.10	P48
57479.26	76.20	g	19.70 ± 0.15	P48
57479.30	76.23	g	19.74 ± 0.17	P48
57480.13	76.81	r	19.54 ± 0.08	P60+SEDM
57480.13	76.81	i	19.43 ± 0.04	P60+SEDM
57480.13	76.81	g	19.81 ± 0.07	P60+SEDM
57480.24	76.88	g	19.58 ± 0.05	P48

Table 1 (cont'd)

MJD (days)	Rest-frame Phase (days)	Filter	AB Mag	Instrument
57480.25	76.89	r	19.51 ± 0.02	P60+SEDM
57480.25	76.89	i	19.41 ± 0.03	P60+SEDM
57480.25	76.89	g	19.77 ± 0.03	P60+SEDM
57480.27	76.91	g	19.70 ± 0.07	P48
57480.31	76.94	g	19.66 ± 0.05	P48
57481.24	77.59	g	19.65 ± 0.07	P48
57481.28	77.61	g	19.62 ± 0.07	P48
57481.33	77.65	r	19.56 ± 0.03	P60+SEDM
57481.33	77.65	i	19.44 ± 0.03	P60+SEDM
57481.34	77.66	g	19.83 ± 0.02	P60+SEDM
57482.23	78.28	g	19.72 ± 0.07	P48
57482.26	78.30	g	19.72 ± 0.08	P48
57482.30	78.33	g	19.75 ± 0.08	P48
57482.34	78.36	r	19.55 ± 0.02	P60+SEDM
57482.34	78.36	i	19.44 ± 0.03	P60+SEDM
57482.34	78.36	g	19.87 ± 0.02	P60+SEDM
57482.35	78.36	u	> 21.02	P60+SEDM
57483.23	78.98	g	19.68 ± 0.07	P48
57483.26	79.01	g	19.77 ± 0.07	P48
57483.30	79.03	g	19.74 ± 0.06	P48
57484.23	79.68	g	19.84 ± 0.11	P48
57484.26	79.71	g	19.89 ± 0.12	P48
57484.27	79.71	r	19.60 ± 0.03	P60+SEDM
57484.28	79.71	i	19.55 ± 0.04	P60+SEDM
57484.28	79.72	g	19.94 ± 0.04	P60+SEDM
57484.29	79.72	r	19.52 ± 0.04	P60+SEDM
57484.29	79.72	i	19.50 ± 0.03	P60+SEDM
57484.29	79.72	g	19.92 ± 0.03	P60+SEDM
57484.30	79.73	g	19.94 ± 0.10	P48
57492.33	85.35	g	20.11 ± 0.12	P48
57493.27	86.01	g	20.18 ± 0.23	P48
57494.25	86.70	g	19.99 ± 0.18	P48
57494.28	86.72	g	20.00 ± 0.22	P48
57495.28	87.42	g	20.09 ± 0.20	P48
57495.32	87.45	r	19.80 ± 0.05	P60+SEDM
57495.33	87.46	i	19.80 ± 0.05	P60+SEDM
57495.34	87.46	g	20.24 ± 0.08	P60+SEDM
57496.28	88.12	g	20.01 ± 0.20	P48
57496.33	88.16	r	19.86 ± 0.06	P60+SEDM
57496.33	88.16	i	19.73 ± 0.04	P60+SEDM
57496.33	88.16	g	20.37 ± 0.07	P60+SEDM
57501.50	91.78	g	> 19.24	P60+SEDM
57501.50	91.78	r	19.66 ± 0.19	P60+SEDM
57504.49	93.88	r	> 19.76	P60+SEDM
57508.18	96.47	g	20.62 ± 0.16	P48
57510.22	97.89	g	20.66 ± 0.17	P48
57510.25	97.91	g	20.52 ± 0.14	P48
57511.19	98.57	g	20.66 ± 0.14	P48
57511.21	98.59	g	20.63 ± 0.14	P48
57511.24	98.61	g	20.71 ± 0.14	P48
57512.18	99.26	g	20.48 ± 0.08	P48
57512.21	99.28	g	20.56 ± 0.12	P48

Table 1 (cont'd)

MJD (days)	Rest-frame Phase (days)	Filter	AB Mag	Instrument
57512.24	99.30	g	20.54 ± 0.10	P48
57513.18	99.96	g	20.78 ± 0.16	P48
57513.20	99.98	g	20.71 ± 0.12	P48
57513.23	100.00	g	20.59 ± 0.12	P48
57513.29	100.04	r	20.17 ± 0.06	P60+SEDM
57513.29	100.04	i	19.91 ± 0.08	P60+SEDM
57513.30	100.05	g	20.87 ± 0.08	P60+SEDM
57518.39	103.61	r	20.25 ± 0.06	P60+SEDM
57518.39	103.62	i	19.99 ± 0.06	P60+SEDM
57518.39	103.62	g	20.87 ± 0.07	P60+SEDM
57519.19	104.17	r	20.35 ± 0.04	P60+SEDM
57519.19	104.17	i	20.11 ± 0.06	P60+SEDM
57519.19	104.18	g	20.86 ± 0.12	P48
57519.19	104.18	g	20.93 ± 0.04	P60+SEDM
57519.21	104.19	g	20.75 ± 0.14	P48
57519.24	104.21	g	20.78 ± 0.10	P48
57520.18	104.87	g	20.92 ± 0.24	P48
57520.20	104.89	g	21.00 ± 0.18	P48
57520.23	104.90	g	20.85 ± 0.20	P48
57521.19	105.58	g	20.91 ± 0.20	P48
57521.22	105.60	g	20.77 ± 0.16	P48
57521.24	105.61	g	20.76 ± 0.15	P48
57522.18	106.27	g	> 20.02	P48
57522.20	106.29	g	> 18.39	P48
57532.35	113.39	r	20.57 ± 0.13	P60+SEDM
57532.35	113.40	i	20.23 ± 0.09	P60+SEDM
57532.35	113.40	g	21.13 ± 0.20	P60+SEDM
57535.31	115.47	r	20.56 ± 0.10	P60+SEDM
57535.31	115.47	i	20.16 ± 0.07	P60+SEDM
57535.32	115.47	g	21.12 ± 0.15	P60+SEDM
57544.17	121.68	r	20.72 ± 0.06	P60+SEDM
57544.18	121.68	g	21.72 ± 0.14	P60+SEDM
57544.24	121.72	r	20.69 ± 0.06	P60+SEDM
57544.25	121.73	g	21.66 ± 0.14	P60+SEDM
57545.22	122.41	g	21.73 ± 0.20	P60+SEDM
57546.27	123.15	r	20.86 ± 0.09	P60+SEDM
57547.18	123.79	r	20.81 ± 0.10	P60+SEDM
57551.31	126.68	r	21.22 ± 0.27	P60+SEDM
57551.31	126.68	g	21.51 ± 0.26	P60+SEDM
57552.54	127.54	uvw2	> 22.90	Swift+UVOT
57552.54	127.54	V	> 19.43	Swift+UVOT
57552.54	127.54	B	> 20.34	Swift+UVOT
57552.54	127.54	u	> 21.05	Swift+UVOT
57552.54	127.54	uvw1	> 22.10	Swift+UVOT
57552.54	127.54	uvm2	> 22.98	Swift+UVOT
57557.25	130.84	r	21.40 ± 0.13	P60+SEDM
57557.25	130.84	g	> 21.84	P60+SEDM
57558.24	131.53	r	> 21.06	P60+SEDM
57558.24	131.54	g	> 21.44	P60+SEDM
57588.17	152.50	r	> 21.46	P60+SEDM
57588.18	152.51	g	> 21.54	P60+SEDM
57592.23	155.35	r	> 21.66	P60+SEDM

Table 1 (cont'd)

MJD (days)	Rest-frame Phase (days)	Filter	AB Mag	Instrument
57592.24	155.36	g	> 21.44	P60+SEDM
57598.20	159.53	r	> 21.16	P60+SEDM
57598.21	159.54	g	> 22.04	P60+SEDM
57605.18	164.42	r	> 21.76	P60+SEDM
57605.19	164.43	g	> 22.24	P60+SEDM
57611.17	168.62	r	> 21.66	P60+SEDM
57611.18	168.63	g	> 21.84	P60+SEDM
57617.14	172.80	r	> 20.36	P60+SEDM
57750.50	266.24	g	24.24 ± 0.15	KeckI+LRIS
57750.50	266.24	r	22.96 ± 0.15	KeckI+LRIS
57828.34	320.77	r	23.87 ± 0.12	DCT
57828.35	320.78	i	23.76 ± 0.13	DCT
57828.36	320.79	g	24.80 ± 0.31	DCT
57840.50	329.29	g	24.68 ± 0.17	KeckI+LRIS
57840.50	329.29	r	24.02 ± 0.13	KeckI+LRIS

Table 2. Summary of Spectroscopic Observations

Observation Date (YYYY MM DD.D)	Phase[a] (rest-frame days)	Telescope+Instrument	Grating[b]	Exp. time[b] (s)	Airmass
2016 Feb 18.5	45.9	Subaru+FOCAS	$\cdots$	600	1.03
2016 Feb 27.5	52.5	P200+DBSP	600/4000, 316/7500	900	1.16
2016 Mar 06.6	58.2	Keck I+LRIS	400/3400, 400/8500	280, 240	1.27
2016 Apr 10.3	82.5	Keck I+LRIS	400/3400, 400/8500	300, 300	1.11
2016 May 05.4	100.1	Keck I+LRIS	400/3400, 400/8500	1200, 1120	1.16
2016 Jun 07.3	123.1	Keck I+LRIS	400/3400, 400/8500	600, 520	1.18
2016 Jun 10.4	125.3	Keck I+LRIS	600/4000, 400/8500	1905, 1800	1.55
2016 Jul 06.3	143.4	Keck I+LRIS	400/3400, 400/8500	2400, 2280	1.64
2017 Jan 02.6	269.6	Keck I+LRIS	400/3400, 400/8500	2730, 2550	1.26
2017 Feb 27.5	308.8	Keck I+LRIS	400/3400, 400/8500	3600, 3510	1.06
2017 Mar 29.4	369.7	Keck I+LRIS	400/3400, 400/8500	5415, 5070	1.09
2017 Apr 29.4	351.4	Keck I+LRIS	400/3400, 400/8500	7200, 7020	1.25

[a] Relative to best-fit explosion date on 2015 December 14.5. To get phase relative to g-band peak, subtract 37.7 days.

[b] Comma-separated values indicate setup for blue and red arms, respectively.

References

1. R. M. Quimby, *et al.*, *Nature* **474**, 487 (2011).
2. A. Gal-Yam, *Science* **337**, 927 (2012).
3. D. Kasen, L. Bildsten, *ApJ* **717**, 245 (2010).
4. S. E. Woosley, *ApJL* **719**, L204 (2010).
5. A. Gal-Yam, *et al.*, *Nature* **462**, 624 (2009).
6. A. Kozyreva, S. Blinnikov, N. Langer, S.-C. Yoon, *A&A* **565**, A70 (2014).
7. S. E. Woosley, S. Blinnikov, A. Heger, *Nature* **450**, 390 (2007).
8. R. A. Chevalier, C. M. Irwin, *ApJL* **729**, L6 (2011).
9. T. J. Moriya, *et al.*, *MNRAS* **428**, 1020 (2013).
10. E. Sorokina, S. Blinnikov, K. Nomoto, R. Quimby, A. Tolstov, *ApJ* **829**, 17 (2016).
11. E. Quataert, J. Shiode, *MNRAS* **423**, L92 (2012).
12. S. E. Woosley, *ApJ* **836**, 244 (2017).
13. L. Yan, *et al.*, *ApJ* **814**, 108 (2015).
14. L. Yan, *et al.*, *ArXiv e-prints* (2017).
15. N. M. Law, *et al.*, *PASP* **121**, 1395 (2009).
16. R. Lunnan, *et al.*, *ArXiv e-prints* (2017).
17. A. De Cia, *et al.*, *ArXiv e-prints* (2017).

18. J. A. Morse, *et al.*, *ApJL* **548**, L207 (2001).

19. A. Tolstov, *et al.*, *ApJ* **835**, 266 (2017).

20. N. Smith, *Nature* **455**, 201 (2008).

21. A. Pastorello, *et al.*, *ApJ* **767**, 1 (2013).

22. J. C. Mauerhan, *et al.*, *MNRAS* **430**, 1801 (2013).

23. F. J. Masci, *et al.*, *PASP* **129**, 014002 (2017).

24. S. B. Cenko, *et al.*, *PASP* **118**, 1396 (2006).

25. N. Blagorodnova, *et al.*, *ArXiv e-prints* (2017).

26. C. Fremling, *et al.*, *A&A* **593**, A68 (2016).

27. C. P. Ahn, *et al.*, **211**, 17 (2014).

28. E. Bertin, *Astronomical Data Analysis Software and Systems XV*, C. Gabriel, C. Arviset, D. Ponz, S. Enrique, eds. (2006), vol. 351 of *Astronomical Society of the Pacific Conference Series*, p. 112.

29. J. B. Oke, *et al.*, *PASP* **107**, 375 (1995).

30. E. F. Schlafly, D. P. Finkbeiner, *ApJ* **737**, 103 (2011).

31. E. Komatsu, *et al.*, *ApJs* **192**, 18 (2011).

32. N. Kashikawa, *et al.*, *PASJ* **54**, 819 (2002).

33. J. B. Oke, J. E. Gunn, *PASP* **94**, 586 (1982).

34. O. Yaron, A. Gal-Yam, *PASP* **124**, 668 (2012).

35. C. Inserra, *et al.*, *ArXiv e-prints* (2016).

36. P. M. Vreeswijk, *et al.*, *ApJ* **797**, 24 (2014).

37. T. Kangas, *et al.*, *MNRAS* **469**, 1246 (2017).

38. M. Nicholl, *et al.*, *MNRAS* **452**, 3869 (2015).

39. M. Nicholl, *et al.*, *Nature* **502**, 346 (2013).

40. M. Nicholl, *et al.*, *ApJ* **826**, 39 (2016).

41. D. A. Howell, *et al.*, *ApJ* **779**, 98 (2013).

42. R. Lunnan, *et al.*, *ApJ* **787**, 138 (2014).

43. D. A. Perley, *et al.*, *ApJ* **830**, 13 (2016).

44. N. N. Chugai, R. A. Chevalier, *ApJ* **641**, 1051 (2006).

45. D. Milisavljevic, *et al.*, *ApJ* **815**, 120 (2015).

46. R. Margutti, *et al.*, *ApJ* **835**, 140 (2017).

47. G. E. Anderson, *et al.*, *MNRAS* **466**, 3648 (2017).

48. M. F. Bietenholz, A. Kamble, R. Margutti, D. Milisavljevic, A. Soderberg, *ArXiv e-prints* (2017).

49. P. Lundqvist, C. Fransson, *ApJ* **464**, 924 (1996).

50. C. Fransson, *et al.*, *ApJ* **336**, 429 (1989).